

Green-Solvent-Processed Inverted Layer-by-Layer Organic Solar Cells Enabled by an Aqueous Soluble Thiophene-alt-Quinoxaline Donor Polymer

Downloaded from: https://research.chalmers.se, 2026-11-24 15:37 UTC

Citation for the original published paper (version of record):
Xiang, J., Jin, Y., Liu, Y. et al (2026). Green-Solvent-Processed Inverted Layer-by-Layer Organic Solar Cells Enabled by an Aqueous
Soluble Thiophene-alt-Quinoxaline Donor Polymer. Solar RRL, 10(20).
http://dx.doi.org/10.1002/solr.70526

N.B. When citing this work, cite the original published paper.

research.chalmers.se offers the possibility of retrieving research publications produced at Chalmers University of Technology. It covers all kind of research output: articles, dissertations, conference papers, reports etc. since 2004. research.chalmers.se is administrated and maintained by Chalmers Library

(article starts on next page)

Check for updates

Solar RRL

RESEARCH ARTICLE OPEN ACCESS

Green-Solvent-Processed Inverted Layer-by-Layer Organic Solar Cells Enabled by an Aqueous Soluble Thiophene-*alt*-Quinoxaline Donor Polymer

Jiale Xiang[1,2] | Yingzhi Jin[3] | Yanfeng Liu[4] | Tadele T. Filate[5] | Zesheng Liu[6] | Jonathan S. Austin[7] | Yuxuan Li[1] | Wendimagegn Mammo[8] | Fan Fu[7] | Feng Gao[1] | Mats Fahlman[6] | Zaifang Li[3] | Niclas Solin[1] | Ergang Wang[5] | Fengling Zhang[1,2]

[1]Department of Physics, Chemistry and Biology, Linköping University, Linköping, Sweden | [2]Wallenberg Initiative Materials Science for Sustainability, Department of Physics, Chemistry and Biology, Linköping University, Linköping, Sweden | [3]College of Biological, Chemical Sciences and Engineering, Jiaxing University, Jiaxing, China | [4]College of Materials and Textile Engineering, Jiaxing University, Jiaxing, China | [5]Department of Chemistry and Chemical Engineering, Chalmers University of Technology, Göteborg, Sweden | [6]Laboratory of Organic Electronics, Department of Science and Technology, Linköping University, Norrköping, Sweden | [7]Laboratory for Thin Films and Photovoltaics, Empa-Swiss Federal Laboratories for Materials Science and Technology, Dübendorf, Switzerland | [8]Department of Chemistry, Addis Ababa University, Addis Ababa, Ethiopia

Correspondence: Ergang Wang (ergang@chalmers.se) | Fengling Zhang (fengling.zhang@liu.se)

Received: 9 July 2026 | **Revised:** 10 October 2026 | **Accepted:** 13 October 2026

Keywords: green solvents | inverted structure | layer-by-layer processing | organic solar cells | solvent orthogonality

ABSTRACT

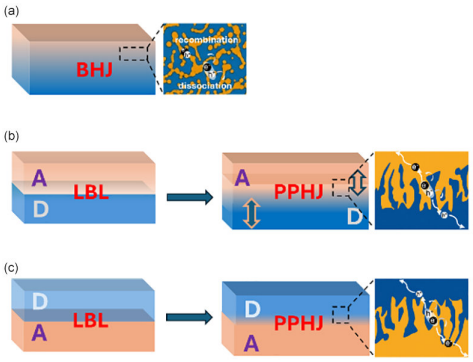
Efficient organic solar cells (OSCs) traditionally rely on bulk heterojunction structures due to the limited exciton diffusion lengths (L_D). The evolution of materials with extended L_D, such as the appearance of nonfullerene acceptors (NFAs), enables sequential layer-by-layer (LbL) processing of electron donor (D) and acceptor (A) a promising strategy for better control over the morphologies of active layers with configuration of D/A in OSCs. However, its application in an inverted structure, that is A/D, remains underexplored, primarily due to the inadequate solvent resistance of small-molecule NFAs, which are prone to dissolved during the solution deposition of the D layer. In this work, we report a fully orthogonal, green-solvent-based LbL strategy for fabricating inverted OSCs using small-molecule NFAs. By pairing a water/ethanol-soluble thiophene-*alt*-quinoxaline-based donor polymer, P(Qx8O-T), with an *o*-xylene-processed acceptor, L8-BO, we successfully suppressed interlayer dissolution, allowing intact deposition of the donor layer without damaging the underlying acceptor film. Furthermore, this strategy effectively maintains the intrinsic crystallization of the donor and NFA layers, resulting in high-quality active layers with well-defined vertical phase separation. Consequently, the green-solvent-processed inverted LbL devices achieve a power conversion efficiency of 5.88%, demonstrating the feasibility of OSCs as a green PV technology.

1 | Introduction

Organic solar cells (OSCs) have attracted significant attention over the past decades due to their flexibility, light weight, low-cost manufacturing, and compatibility with large-area solution processing [1–5]. Though the bulk heterojunction (BHJ) structures, generally with polymer donors (PDs) and nonfullerene acceptors (NFAs), have pushed the power conversion efficiency (PCE) of OSCs beyond 20% [6–12], it has still significant limitations to be addressed. PDs and NFAs form randomly interpenetrating networks within BHJ structures, which facilitate charge generation as exciton diffusion lengths in organic materials are restricted to approximately 10 nm (Scheme 1a) [13–15]. While a large interfacial area favors exciton dissociation, the disordered

This is an open access article under the terms of the Creative Commons Attribution License, which permits use, distribution and reproduction in any medium, provided the original work is properly cited.

© 2026 The Author(s). *Solar RRL* published by Wiley-VCH GmbH.



SCHEME 1 | Donor and acceptor distribution in (a) BHJ, (b) conventional PPHJ, and (c) inverted PPHJ by LbL deposition.

nature of the pathways often leads to significant charge recombination, hindering efficient charge transport and extraction. Besides, the randomly distributed nature of BHJ leads to uncontrolled phase separation, morphological instability, and limited reproducibility [16–18].

Recently, the development of novel materials with extended exciton diffusion lengths, such as Y-series acceptors [19, 20], has paved the way for layer-by-layer (LbL) sequential deposition, which yields a pseudo-planar heterojunction (PPHJ) structure and effectively suppress charge recombination (Scheme 1b). It offers better control over the vertical composition, layer thickness, and crystalline morphology of the deposited donor and acceptor layers independently compared to BHJ structure [21–29].

However, the pursuit of high-performance LbL devices is currently hindered by two major bottlenecks: device architecture and environmental sustainability. First, while inverted structures are favored for industrial stability, fabricating them via LbL remains challenging (Scheme 1c). The NFA layer, typically composed of small molecules and deposited first in inverted setups, is highly susceptible to interfacial erosion by the subsequent donor-layer solvent [30]. Second, the majority of current high-efficiency systems still rely on toxic halogenated solvents, such as chloroform (CF) and chlorobenzene (CB), posing significant environmental and health risks that impede large-scale manufacturing [31–35]. Besides, the economic viability of large-scale OSC manufacturing is influenced by solvent costs and post-processing waste management. Traditional halogenated solvents not only necessitate strict safety protocols but also incur significant costs associated with specialized disposal and recycling. Therefore, developing effective and high-performance green-processing strategies is urgently to be explored in the OSC field [36–40].

To address above bottleneck, researchers have strived to design and synthesize new photovoltaic materials compatible with greener solvents [41–44], particularly mixtures of ethanol and water, which are considered among the least hazardous. The common strategy involves incorporating oligo(ethylene glycol) (OEG) side chains into the conjugated polymer backbone [45–47]. Pioneer work, such as by You et al., systematically investigated the effect of OEG side chain architecture on green-solvent solubility/processability, demonstrating that branched OEG side chains (e.g., PTQ-6bO/6bO2 derivatives) significantly improve solubility compared to linear OEG architectures and successfully applied the PTQ-6O derivative in BHJ devices to get a PCE of 6.2% [48]. Wang and coauthors contributed to this effort by developing a low-cost quinoxaline-based polymer, P(Qx8O-T) [49], which features a simple synthetic route and a deep highest occupied molecular orbital (HOMO) level, making it highly promising for green-solvent processing. However, when combined with the aqueous-soluble polymer acceptor P(NDIDEG-T) in a BHJ structure, the resulting device exhibited a limited PCE of 2.27%. This limited performance was mainly attributed to the noncomplementary absorption spectrum and the nonsatisfactory interpenetrating donor/acceptor morphology resulting from the inherent difficulty in controlling the phase separation of BHJ blends.

Herein, a fully orthogonal solvent system was developed to fabricate inverted devices via the LbL strategy, utilizing water/ethanol-soluble P(Qx8O-T) as the donor and L8-BO as the acceptor. This approach effectively circumvents the problematic phase-separation issues inherent in green-solvent-processed BHJ blends. Comprehensive characterization of morphology and physical properties confirmed that this new method achieves independent control over film formation and crystallization of donor and acceptor, preserving pristine crystalline domains while maintaining sufficient interfacial contact for exciton dissociation and carrier transport. This structural optimization led to improved carrier mobility and effectively reduced recombination losses. Furthermore, the optimized surface morphology was found to improve the contact behavior between active layer and electrode, increasing the carrier extraction efficiency. The champion devices demonstrated a high PCE of 5.88%. This work demonstrates a generalizable strategy to unlock incompatible donor/acceptor pairs for green-processed, high-performance inverted OSCs.

2 | Results and Discussion

2.1 | Optoelectronic Properties

Figure 1a shows the chemical structures of the water/ethanol-soluble donor polymer P(Qx8O-T) and the small-molecule acceptor L8-BO. As schematically depicted in Supporting Information, Figure 1 (Figure S1), the active layers were fabricated through a LbL strategy, where the acceptor was first deposited from *o*-xylene, a nonhalogenated solvent, followed by deposition of the donor from water/ethanol solutions. Figures 1b and S2 present the energy levels of the two materials determined by a combination of ultraviolet photoelectron spectroscopy (UPS) and UV–vis absorption spectroscopy. The HOMO levels, derived from the UPS secondary electron cutoff and valence band onset, are −5.28 eV for P(Qx8O-T) and −5.48 eV for L8-BO.

Figure 1c presents the UV–vis absorption spectra of P(Qx8O-T) (black), L8-BO (red), bilayer L8-BO/P(Qx8O-T) (blue), and bilayer L8-BO/PTQ10 (green). P(Qx8O-T) and L8-BO display highly complementary absorption spectra, with the maximum absorption peak at 599 and 804 nm, respectively. To evaluate the solvent orthogonality of the LbL process, we first compared the stability of the predeposited L8-BO layer upon deposition of the donor layer using different processing solvents. As shown in

2367198x, 2026, 20, Downloaded from https://onlinelibrary.wiley.com/doi/10.1002/solr.70526 by Chalmers Research - Chalmers University Of Technology , Wiley Online Library on [29/10/2026]. See the Terms and Conditions (https://onlinelibrary.wiley.com/terms-and-conditions) on Wiley Online Library for rules of use; OA articles are governed by the applicable Creative Commons License

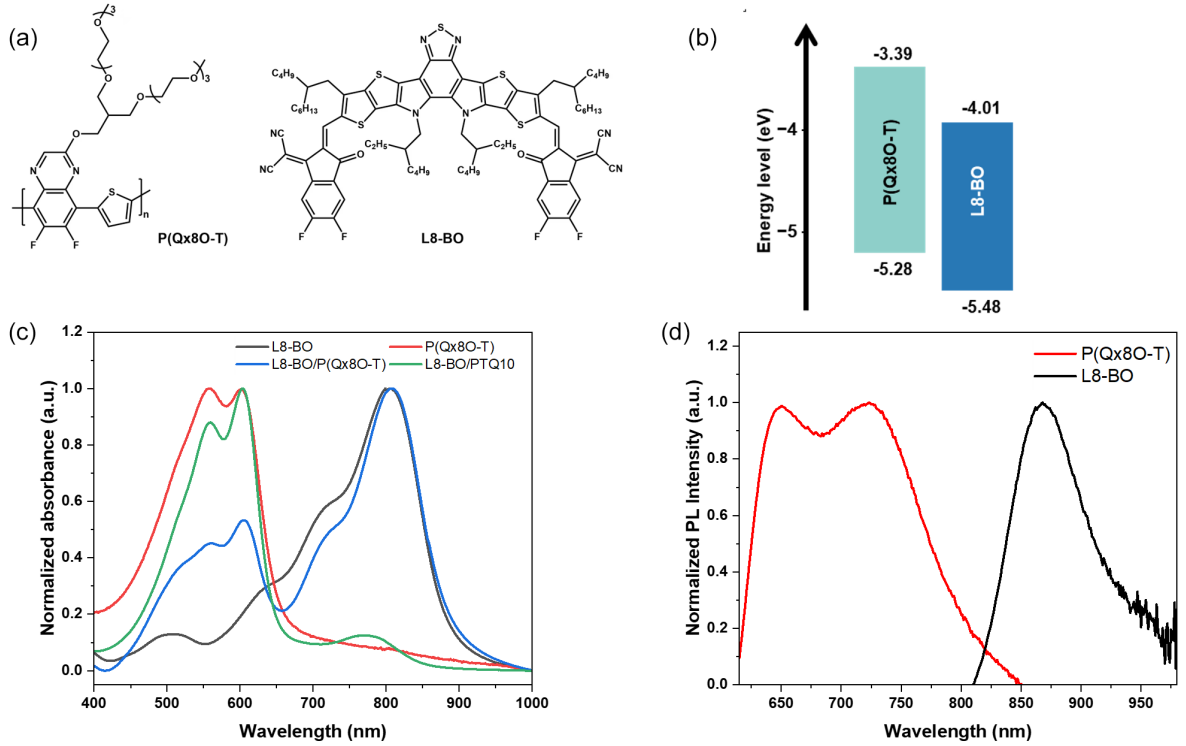


FIGURE 1 | (a) Chemical structures of P(Qx8O-T), L8-BO. (b) Energy alignment of P(Qx8O-T), L8-BO. (c) Absorption spectra of four films (L8-BO, P(Qx8O-T), bilayer L8-BO/P(Qx8O-T) and bilayer L8-BO/PTQ10. (d) Steady-state PL spectra of pristine L8-BO and P(Qx8O-T) films.

Figure 1c, deposition of PTQ10 from chloroform (the chemical structure is shown in Figure S3) substantially suppresses the characteristic absorption of L8-BO, indicating severe erosion of the underlying acceptor layer. In contrast, the characteristic L8-BO absorption is largely preserved after deposition of P(Qx8O-T) from a water/ethanol mixture. This observation is further supported by direct solvent treatment experiments, which show negligible changes in the L8-BO absorption and film thickness after exposure to the water/ethanol mixture (Figure S4 and Table S1), demonstrating good compatibility of the water/ethanol system with the predeposited L8-BO layer. To further investigate the photophysical properties of the pristine materials, steady-state photoluminescence (PL) spectra were recorded under 600 and 800 nm excitation for P(Qx8O-T) and L8-BO, respectively. As shown in Figure 1d, the pristine P(Qx8O-T) and L8-BO films exhibit emission peaks at approximately 725 and 870 nm, respectively.

2.2 | The Vertical Distributions of Films

To elucidate the vertical distribution of P(Qx8O-T) within the active layers, PL measurements were performed by exciting either the front- or rear side of the films (Figure S5). Since the PL signals are primarily generated from the side of incident light, this approach serves as a sensitive probe for spatial phase distribution. As shown in Figure 2a, the PL spectra of the BHJ films were consistently dominated by L8-BO emission regardless of the excitation direction, indicating that the donor and acceptor domains were thoroughly intermixed throughout the entire film. In contrast, the PL spectra of a PPHJ film exhibited significant dependence on the excitation directionality (Figure 2b). Emission of P(Qx8O-T) ranging from 600 to 800 nm was observed when excited from the front side but completely disappeared under rear-side excitation because excitation light was mostly absorbed by L8-BO and less reached to P(Qx8O-T) layer. Consistent with the PL peaks of

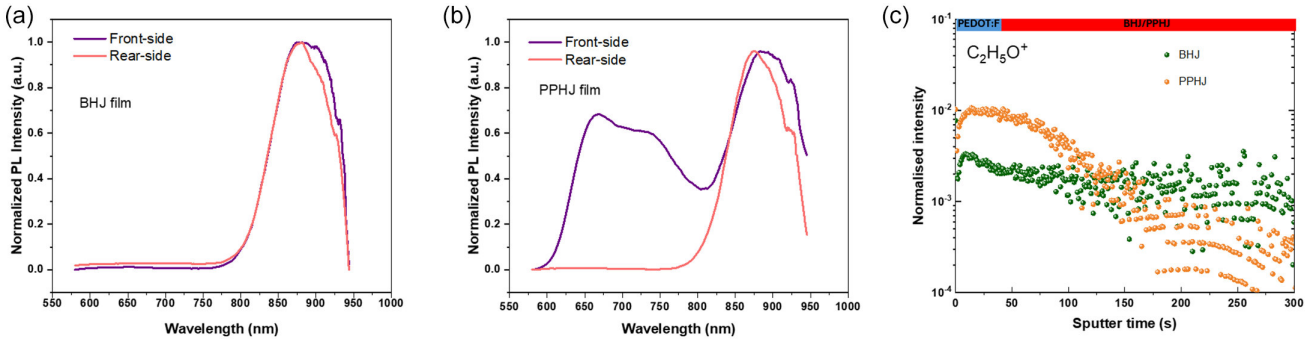


FIGURE 2 | The PL spectra of the 2 films with (a) BHJ and (b) PPHJ architectures, which were excited from the front- and rear-sides. (c) ToF-SIMS depth profiling of BHJ and PPHJ films, showing normalized intensity of $C_2H_5O^+$ signal – attributed to P(Qx8O-T).

2367198x, 2026, 20, Downloaded from https://onlinelibrary.wiley.com/doi/10.1002/solr.70526 by Chalmers Research - Chalmers University Of Technology , Wiley Online Library on [29/10/2026]. See the Terms and Conditions (https://onlinelibrary.wiley.com/terms-and-conditions) on Wiley Online Library for rules of use; OA articles are governed by the applicable Creative Commons License

the pristine films, this disparity demonstrates the presence of a vertically stratified structure in the PPHJ film. Specifically, the front side exhibits a P(Qx8O-T)-enriched surface, whereas the rear side comprises L8-BO-enriched domains, in stark contrast to the uniformly mixed nature throughout the BHJ bulk.

To further validate the differences in vertical composition of BHJ and PPHJ films, time-of-flight secondary ion mass spectrometry (ToF-SIMS) was employed (Figure 2c). The $C_2H_5O^+$ group was used to track P(Qx8O-T). The interface between the PEDOT:F (hole transport layer, HTL) and the active layer was identified at a sputter time of ~30 s (defined by the 86% threshold of the C^+ signal). Notably, the depth profile of the BHJ film remained relatively flat, indicating a disordered and homogeneous distribution of components. However, the PPHJ film exhibited an obvious enrichment of P(Qx8O-T) in the top region. The high P(Qx8O-T) intensity at the very beginning of the profile suggests a degree of intermixing between the donor and the HTL. As the sputter depth increased, the donor concentration in the PPHJ film decreased sharply, confirming a transition from a donor-enriched surface to a mixed bulk region. This stratified vertical architecture, which comprises a P(Qx8O-T)-rich top and a balanced mixed sublayer, benefits from suppressing bimolecular recombination and enhancing charge collection. The comparative vertical morphologies of BHJ and PPHJ architecture are further illustrated in Scheme 1.

2.3 | Photovoltaic Performance

To unlock the full potential of the aqueous processability of the donor polymer in fully orthogonal solvents that can conserve the integrity of the underlying acceptor films, we fabricated OSCs with an inverted architecture in both BHJ and PPHJ devices. The corresponding device architecture is illustrated in Figure S6, adopting an inverted structure with ITO/Zn–PEIE/active layer/PEDOT:F/Ag. In addition, Zn-PEIE serves as a solution-processable electron transport layer that eliminates the need for ultraviolet light activation while improving cathode contact [50]. Meanwhile, PEDOT:F, a doped conjugated polymer dissolved in ethanol, is utilized as the HTL [51].

Figure 3a presents the current density–voltage (*J*–*V*) characteristics of the resulting OSCs under AM 1.5G illumination at 100 mW cm^{-2}. The corresponding photovoltaic parameters are summarized in Table 1. The statistical data are shown in Figure S7 and Table S2. The BHJ OSCs achieved a PCE of 4.11%, with an open-circuit voltage (V_{OC}) of 0.58 V, a short-circuit current density (J_{SC}) of 16.37 mA cm^{-2}, and a fill factor (*FF*) of 43.65%. In contrast, the inverted PPHJ devices delivered a superior *PCE* of 5.88%, with V_{OC} of 0.63 V, J_{SC} of 17.51 mA cm^{-2}, and FF of 53.05%. For comparison, the photovoltaic performance of the conventional PPHJ device is provided in Figure S8, which shows a lower PCE of 4.28% than that of the inverted PPHJ device. The relatively lower PCE of the conventional devices is likely associated with the less favorable interfacial and charge-extraction characteristics of the PEDOT:PSS-based architecture under the aqueous/ethanol processing conditions. Therefore, the inverted architecture was selected for subsequent studies due to its better compatibility with the orthogonal solvent processing strategy and improved device performance.

This direct comparison of OSCs with different active-layer architectures reveals that the PPHJ structure significantly enhanced both V_{OC} and J_{SC}, leading to a markedly improved overall device performance. While thermal annealing is known to exert a profound influence on the morphology of PPHJ OSCs, its systematic optimization is beyond the scope of this work and will be addressed in future reports.

The external quantum efficiency (EQE) spectra of the two OSCs (Figure 3b) also showed consistency with above results. The PPHJ OSC exhibited higher EQE in visible and near-infrared regions, particularly in the absorption range of L8-BO, leading to an integrated current density of 17.48 mA cm^{-2}, in good agreement with the measured J_{SC}. By contrast, the BHJ OSC exhibits weaker photoresponse with an integrated J_{SC} of 16.11 mA cm^{-2}. The wavelength-dependent EQE response can be understood in terms of the distinct vertical phase distributions of the BHJ and PPHJ architectures. In the inverted PPHJ device, P(Qx8O-T) is preferentially enriched toward the top surface, implying a corresponding L8-BO-enriched region toward the bottom, whereas the BHJ exhibits a relatively homogeneous donor/acceptor distribution. Since light enters from the ITO side, the vertical phase distribution can influence the optical path and the spatial distribution of photogeneration. In the 400–500 nm region, where P(Qx8O-T) contributes substantially to the photoresponse, part of the incident light may be attenuated before reaching the P(Qx8O-T)-rich upper region, which may contribute to the slightly lower EQE of the PPHJ device compared with the BHJ device. In contrast, at longer wavelengths, particularly in the L8-BO absorption region, the L8-BO-enriched lower region is directly exposed to the incident light, which may facilitate photon absorption and photogeneration in the L8-BO-rich region. Together with the more favorable charge-generation and extraction pathways enabled by the vertically stratified morphology, this contributes to the enhanced EQE of the PPHJ device at longer wavelengths. These findings confirm that the orthogonal LbL strategy not only prevented interlayer dissolution but also promoted more efficient photon-to-electron conversion, thereby enhancing both photocurrent and overall device efficiency.

To gain deeper insight into the origin of the performance enhancement, the fundamental electrical characteristics of the devices were first examined. Dark *J*–*V* curves were analyzed to evaluate diode quality and leakage behavior. As shown in Figure S9, the PPHJ devices exhibited suppressed leakage current and higher ideality factor, compared to BHJ devices. The charge recombination kinetics were further investigated through light-intensity (P_{light})-dependent measurements. For the PPHJ devices, as depicted in Figure S10, the power-law exponent α, extracted from $J_{SC} \propto P_{light}^{\alpha}$, reached the value of 0.97, exceeding that of BHJ devices (0.95). This slightly higher α value indicates more efficient charge extraction and suppressed bimolecular recombination under short-circuit conditions. Furthermore, the dependence of V_{OC} on illuminated light intensity P_{light} was analyzed to evaluate the ideality factor (n), extracted from the slope of kT/q, where k is the Boltzmann constant, T is the temperature and q is the elementary charge, respectively. Generally, the value of n ranges between 1 and 2, and a value closer to 2 indicates more severe trap-assisted recombination. The BHJ devices showed a higher value of 1.75 kT/q, implying severe recombination losses,

2367198x, 2026, 20, Downloaded from https://onlinelibrary.wiley.com/doi/10.1002/solr.70526 by Chalmers Research - Chalmers University Of Technology , Wiley Online Library on [29/10/2026]. See the Terms and Conditions (https://onlinelibrary.wiley.com/terms-and-conditions) on Wiley Online Library for rules of use; OA articles are governed by the applicable Creative Commons License

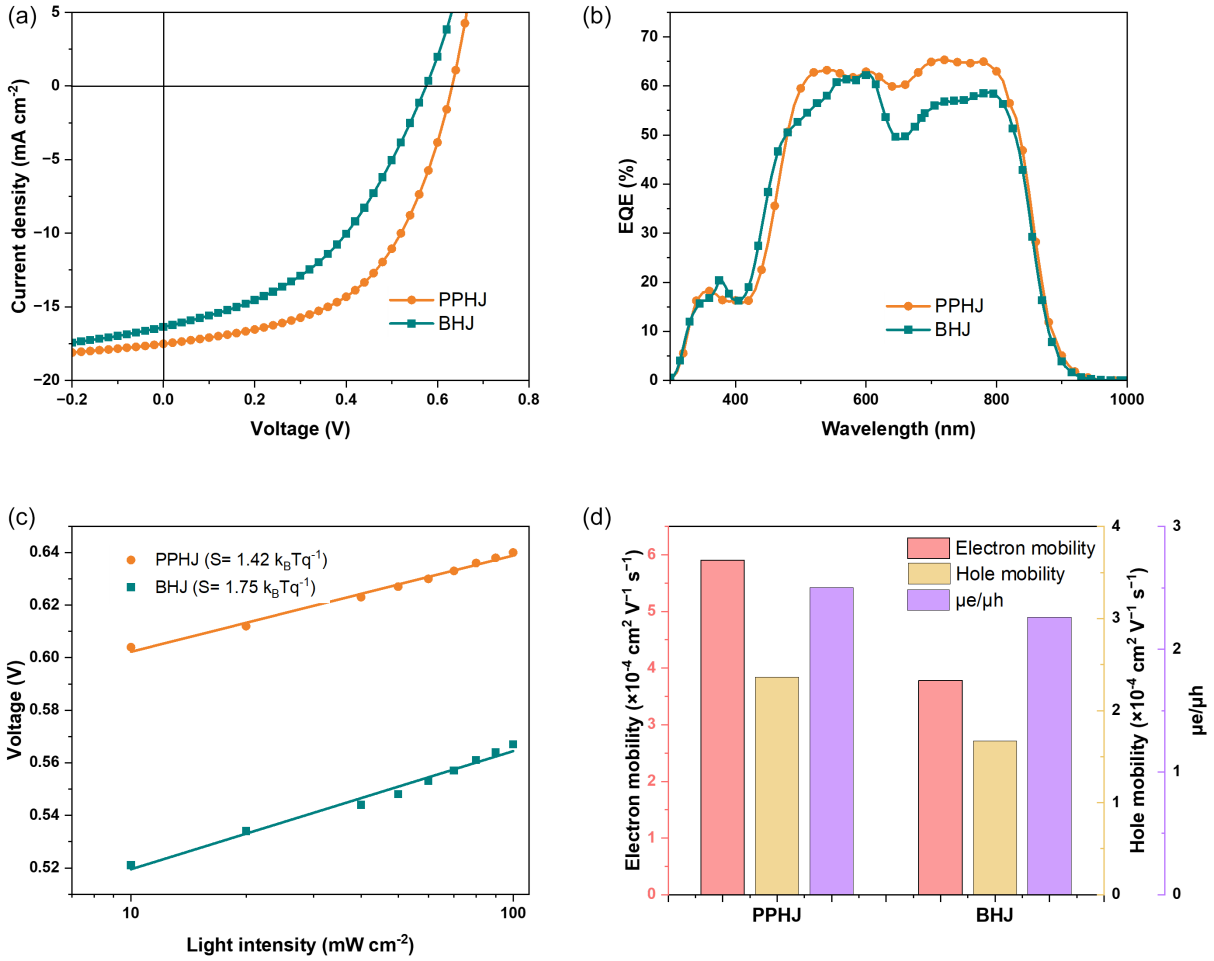


FIGURE 3 | (a) *J–V* curves, (b) EQE spectra, (c) V_{OC} dependence on light intensity and (d) charge mobilities of OSCs with two different architectures.

TABLE 1 | Photovoltaic parameters of OSCs with BHJ and PPHJ architectures.

	V_{OC}, V	J_{SC}, mA/cm^2	Cal. J_{SC}[a], mA/cm^2	FF, %	PCE[b], %
PPHJ	0.63	17.51	17.48	53.05	5.88
	(0.63 ± 0.02)	(16.28 ± 0.92)		(50.34 ± 2.05)	(5.16 ± 0.46)
BHJ	0.58	16.37	16.11	43.65	4.11
	(0.57 ± 0.04)	(15.03 ± 0.90)		(43.58 ± 1.92)	(3.71 ± 0.29)

[a]Cal. J_{SC} represents the integrated current density obtained from EQE spectra.
[b]The values in parentheses are the average ± standard deviation obtained from 15 devices.

whereas the PPHJ devices exhibited a significantly reduced slope of 1.42 kT/q, suggesting a mitigated trap-assisted recombination (Figure 3c). Taken together, both the higher α and lower n in PPHJ devices corroborated the superior charge extraction and reduced recombination losses, consistently accounting for the enhanced FF observed in these devices. A likely explanation is the improved morphology of the active layer in the PPHJ OSCs, which will be discussed in detail later (Section 2.4). Meanwhile, as shown in Figure S11, the exciton dissociation probability (P_{diss}) of the PPHJ OSC was 0.88, higher than that of the BHJ devices (0.83). However, this value remains suboptimal, which accounts for the relatively modest J_{SC} observed in these devices.

The space–charge-limited current (SCLC) was employed to measure the charge carrier mobility in devices, providing quantitative insight into how the LbL-induced vertical phase separation affects the charge transport kinetics. As shown in Figures 3d and S12, the mobilities of the electron (μ_e) and hole (μ_h) in the PPHJ OSC were 5.90×10^{-4} cm^2 V^{-1} S^{-1} and 2.36×10^{-4} cm^2 V^{-1} S^{-1}, respectively, which are higher than those in BHJ OSCs (3.78×10^{-4} cm^2 V^{-1} S^{-1} and 1.67×10^{-4} cm^2 V^{-1} S^{-1}). The differences in charge transport behaviors come from the different morphological organizations of the two systems. In BHJ films, the disordered interpenetrating network often creates fragmented pathways, which limit charge mobility and increase the likelihood of trap-assisted recombination at domain boundaries. Conversely, the PPHJ architecture fosters larger, continuous pure domains that preserve the intrinsic high mobilities of both the donor and acceptor. Consequently, PPHJ devices exhibit enhanced absolute mobility values compared to BHJ counterparts. Although the μ_e/μ_h ratio was slightly higher in PPHJ (2.50 vs. 2.26 for BHJ), this slight asymmetry did not lead to significant space–

2367198x, 2026, 20, Downloaded from https://onlinelibrary.wiley.com/doi/10.1002/solr.70526 by Chalmers Research - Chalmers University Of Technology , Wiley Online Library on [29/10/2026]. See the Terms and Conditions (https://onlinelibrary.wiley.com/terms-and-conditions) on Wiley Online Library for rules of use; OA articles are governed by the applicable Creative Commons License

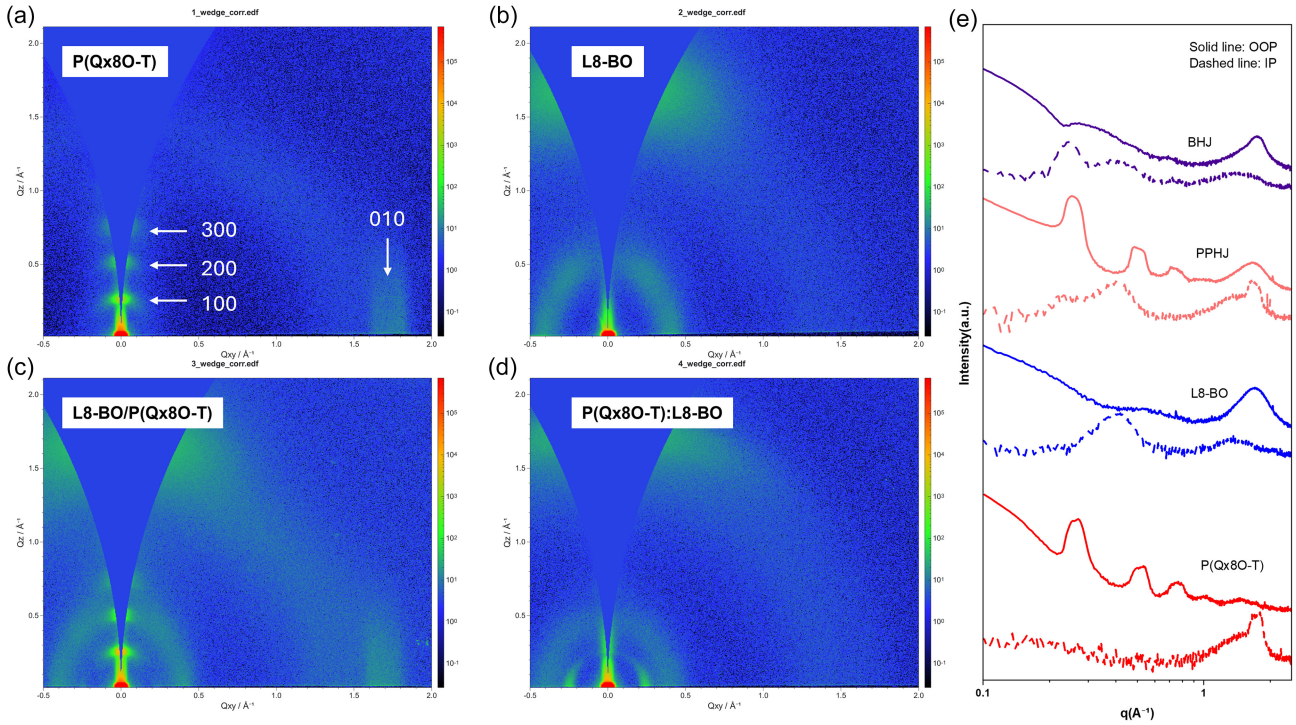


FIGURE 4 | 2D GIWAXS patterns of (a) P(Qx8O-T), (b) L8-BO, (c) L8-BO/P(Qx8O-T) with LbL deposition, and (d) L8-BO:P(Qx8O-T) blend films. (e) 1D GIWAXS plot.

charge accumulation. The faster carrier extraction afforded by the elevated mobilities outcompeted recombination losses, preserving the photocurrent at high bias voltages and thereby sustaining a higher *FF*.

2.4 | Morphology Analysis

To elucidate the fundamental reasons behind the variations in performance for BHJ and PPHJ OSCs, comprehensive investigations on morphology were conducted. The contact angle measurement was employed to investigate the compatibility between P(Qx8O-T) and L8-BO. As shown in Figure S13, the surface energy (γ) of P(Qx8O-T) and L8-BO are 88.97 and 25.29 mN m^{-1}, respectively, suggesting the two materials are incompatible in mixing together. Due to the significant surface energy mismatch between P(Qx8O-T) and L8-BO, the BHJ films undergo excessive phase separation, resulting in a substantial increase in surface roughness (Figure S14), leading to unfavorable physical contact between the active layer and the electrodes. In contrast, in PPHJ films, the top surface, primarily composed of pure donor, exhibited a significantly reduced root–mean-square (RMS) roughness of 1.54 nm. This superior surface planarity ensures optimized interfacial contact and suppresses charge recombination at the electrode interface, thereby enhancing the overall device performance.

Grazing incidence wide-angle X-ray scattering (GIWAXS) measurements were adopted to investigate the structural differences regarding the molecular packing between the two films. The 2D diffraction patterns and 1D line-cut profiles are illustrated in Figure 4. Table 2 presents detailed information on the d-spacing, peak area, and crystal coherence length (CCL) of the (100) and (010) peaks in the films. As shown in Figure 4a,b, neat films of both P(Qx8O-T) and L8-BO exhibited high crystalline order. The P(Qx8O-T) polymer molecules exhibited a preferred edge-on stacking. The (100) diffraction peak was located at out-of-plane (OOP) directions at $q = 0.26\ \text{Å}^{-1}$ and the (010) diffraction peak was found at $q = 1.75\ \text{Å}^{-1}$ in the in-plane (IP) direction, corresponding to d-spacing of 24.16 and 3.59 Å, respectively. The CCL of (100) and (010) are 145.2 and 25.2 Å, respectively, indicating a long-range order in the lamellar stacking direction. And the L8-BO molecules exhibited a preferred face-on stacking, with (010) diffraction peak located at OOP direction ($q = 1.71\ \text{Å}^{-1}$, $d = 3.68$ Å). In blend films, though the BHJ film exhibits a more compact $\pi - \pi$ stacking ($d_{010} = 3.61$ Å) compared to the PPHJ film ($d_{010} = 3.74$ Å), it suffers from significantly lower crystallinity and reduced CCL, indicating that the large surface energy mismatch between the hydrophilic donor and hydrophobic acceptor disrupts the molecular self-assembly. And characterized by a sharp (100) lamellar peak ($d_{100} = 24.17$ Å) and a large CCL (168.3 Å), a high crystallinity of PPHJ film is well maintained, indicating the independent crystallization during the LbL deposition process. In contrast, the BHJ film exhibits a dramatic loss of order, with the (100) peak intensity and CCL dropping by orders of magnitude. This loose packing in the BHJ, along with the high surface roughness (3.81 nm), leads to inferior charge transport and rapid recombination, whereas the LbL process preserves a more ordered and compact crystalline framework conducive to higher device performance.

2.5 | Exciton Dissociation Kinetics

Time-resolved PL (TRPL) measurements were performed to study the exciton harvesting and dissociation kinetics in the

2367198x, 2026, 20, Downloaded from https://onlinelibrary.wiley.com/doi/10.1002/solr.70526 by Chalmers Research - Chalmers University Of Technology , Wiley Online Library on [29/10/2026]. See the Terms and Conditions (https://onlinelibrary.wiley.com/terms-and-conditions) on Wiley Online Library for rules of use; OA articles are governed by the applicable Creative Commons License

TABLE 2 | Detailed data of GIWAXS characterization.

Structure	(010)			(100)		
	Position ($Å^{-1}$)	Distance (Å)	CCL (Å)	Position ($Å^{-1}$)	Distance (Å)	CCL (Å)
BHJ	1.74	3.61	23.7	—	—	—
PPHJ	1.68	3.74	26.8	0.26	24.17	168.3

films. The P(Qx8O-T), L8-BO, and P(Qx8O-T)/L8-BO films in both BHJ and PPHJ architecture were excited at 645 nm by a laser to obtain TRPL spectra. The PL decay plots of blend and neat films are shown in Figure S15. The BHJ and PPHJ films both exhibited PL decay faster than the neat films at 680 and 880 nm. This rapid quenching indicates efficient exciton diffusion to the donor/acceptor interface, followed by subsequent charge transfer. Specifically, in PPHJ film, the lifetime of PL decay recorded at 680 and 880 nm were both longer than those in BHJ film, implying longer exciton lifetime in both P(Qx8O-T) and L8-BO domains. This distinction can be attributed to the differences in morphology between the two films. In BHJ films, the high interface density and intimate intermixing facilitate near-instantaneous quenching, which may act as excessive charge recombination centers, while in PPHJ films, the presence of more pristine P(Qx8O-T) crystalline domains allows excitons to reside longer within the pure phases before reaching a dissociation site at the donor/acceptor interface. This balanced exciton lifetime in the PPHJ film indicates a better morphology where pure P(Qx8O-T) and L8-BO domains provide efficient pathways for charge transport, while the P(Qx8O-T)/L8-BO interfacial region ensures sufficient charge generation. Thus, the orthogonal LbL strategy provides promising opportunities for control of morphology and balanced charge transport, resulting in enhanced V_{OC}, efficient charge extraction, and overall higher device efficiency.

2.6 | Film Formation Dynamics

To gain qualitative insight into the transient molecular assembly and crystallization processes, model in situ absorption measurements were performed during film deposition. These measurements were intended to compare the relative film formation behavior of the BHJ and LbL systems rather than to quantitatively reproduce the absolute kinetics under device-fabrication conditions. Figure 5a–c presents the time-dependent UV–vis absorption contour maps for P(Qx8O-T), BHJ, and PPHJ, respectively. The intensity profile at 599 nm, corresponding to the characteristic absorption peak of P(Qx8O-T), was extracted to investigate the solidification dynamics (Figure 5d–f). Generally, the evolution of the absorption profiles can be categorized into three distinct stages: solvent evaporation (stage 1, orange region in Figure 5d–f), solute precipitation/crystallization (stage 2, red region), and dry film formation (stage 3, blue region) [18, 52]. The second stage, characterized by a pronounced intensity enhancement in the absorption spectra, is critical for defining the molecular aggregation and phase separation. As shown in Figure 5d–f, a significant difference in crystallization kinetics was observed between the BHJ and PPHJ systems. In the BHJ films (processed with chloroform), stage 2 was rapid, with solidification completed within 6 s (from 25 to 31 s). This nearly instantaneous quenching restricts the time available for molecular self-organization, leading to a more disordered bulk morphology with limited crystallinity. In contrast, the LbL-processed P(Qx8O-T)

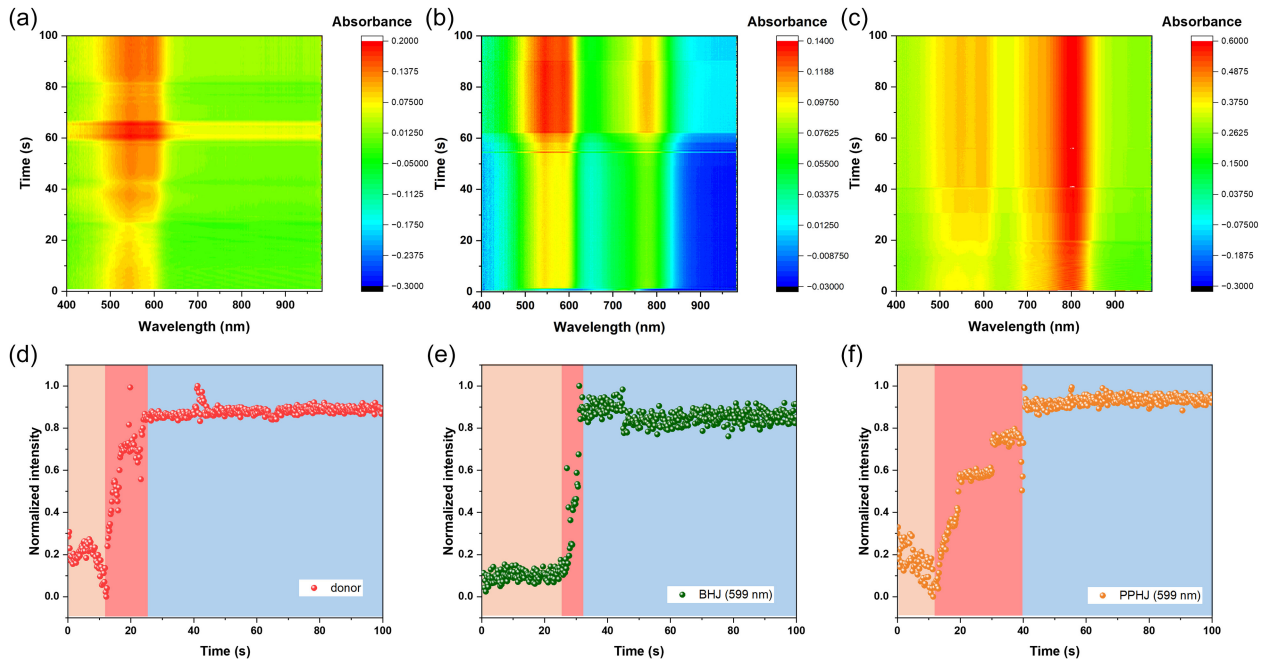


FIGURE 5 | In situ 2D absorption spectra of (a) P(Qx8O-T), (b) L8-BO:P(Qx8O-T) and (c) L8-BO/P(Qx8O-T). Intensity evolution at 599 nm versus time for (d) P(Qx8O-T), (e) L8-BO:P(Qx8O-T) and (f) L8-BO/P(Qx8O-T).

2367198x, 2026, 20, Downloaded from https://onlinelibrary.wiley.com/doi/10.1002/solr.70526 by Chalmers Research - Chalmers University Of Technology , Wiley Online Library on [29/10/2026]. See the Terms and Conditions (https://onlinelibrary.wiley.com/terms-and-conditions) on Wiley Online Library for rules of use; OA articles are governed by the applicable Creative Commons License

film exhibited a significantly prolonged crystallization process (~29 s, from 12 to 41 s), which is not only longer than that in the BHJ blend but also exceeds the solidification time of the neat P(Qx8O-T) film on a bare substrate (~12 s, from 12 to 24 s). This extended kinetic window provides a longer period for molecular relaxation and ordering, which is consistent with the enhanced crystalline order observed in the GIWAXS measurements. Notably, the growth profile of LbL-processed P(Qx8O-T) film revealed a unique stepwise intensity increase, a feature absent in both the BHJ and neat P(Qx8O-T) films. This stepwise kinetics is likely associated with the selective evaporation of the water/ethanol cosolvent and its interaction with the underlying L8-BO layer. Since P(Qx8O-T) has lower solubility in water, the faster evaporation of ethanol creates a self-regulating antisolvent effect within the residual liquid. Simultaneously, the swelling effect of the solvent on the underlying L8-BO layer, which traps residual solvent molecules at the donor/acceptor interface, slows down the final stabilization. This modulated, multistage growth ensures an intimate donor/acceptor contact while preserving high crystallinity, ultimately explaining the simultaneous enhancement in J_{SC} and *FF* for PPHJ devices.

To further corroborate the film formation mechanisms, in situ PL spectroscopy was employed to monitor the real-time evolution of excited-state dynamics during the film formation processes (Figure S16). As shown in Figure S16a, the time-dependent PL contour map of the L8-BO/P(Qx8O-T) bilayer exhibits a three-stage quenching trend, which is highly consistent with the film-formation kinetics observed in the in situ absorption spectra. In the initial solvent evaporation stage, a broad and relatively intense PL signal is observed, corresponding to the polymer or small molecules in a solvated, disordered state. As the process enters the nucleation and crystallization stage, a red shift in the PL peak position occurs, accompanied by a progressive change in emission intensity. This shift reflects the transition from isolated chains to aggregated molecular packing, where restricted molecular rotation and enhanced interchain interactions redefine the radiative recombination pathways. In the final dry film stage, as shown in Figure S16b, the incomplete quenching of the P(Qx8O-T) emission indicates the formation of pristine P(Qx8O-T) phases, which is in good agreement with the ToF-SIMS results. Furthermore, the temporal lag in L8-BO quenching relative to P(Qx8O-T) (Figure S16c) suggests a solvent-induced swelling effect on the L8-BO layer, followed by a gradual molecular infiltration of P(Qx8O-T) into the underlying matrix. The PL profiles signify the formation of a robust, highly ordered PPHJ network, where the optimized vertical phase separation effectively balances exciton diffusion and charge transfer at the P(Qx8O-T)/L8-BO interface.

3 | Conclusions

In summary, this study demonstrates a fully orthogonal green solvent processing strategy to fabricate inverted OSCs with a PPHJ architecture. By employing a water/ethanol-soluble donor, P(Qx8O-T), and an o-xylene-processed NFA, L8-BO, we successfully addressed the challenge of processing donor–acceptor systems with extreme polarity differences. Compared with the BHJ reference, the orthogonal LbL strategy enables more controlled film formation, reduced surface roughness, and favorable molecular packing. The in situ optical characterizations reveal that the LbL-processed donor undergoes a prolonged crystallization period, which is consistent with the formation of highly ordered crystalline films. Furthermore, the donor solution exerts a controlled swelling and infiltration effect on the underlying acceptor layer, ultimately facilitating the evolution of a PPHJ architecture. TOF-SIMS and GIWAXS analysis confirm that the LbL process preserves the intrinsic high crystallinity of the donor while establishing a favorable vertical composition gradient. Although the edge-on orientation constrains the vertical charge mobility to the 10^{-4} cm^2 V^{-1} S^{-1} range and maintains a moderate P_{diss} (~0.88), the resulting transport pathways and charge extraction characteristics enable the PPHJ device to outperform the BHJ reference under their respective optimized processing conditions, achieving a PCE of 5.88%. This work provides a sustainable and potentially scalable pathway for the development of low-cost, high-performance OSCs through strategic interface and morphology engineering in green solvent systems.

4 | Experimental Section

4.1 | Materials

All materials except the P(Qx8O-T) were purchased from commercial suppliers. Zinc acetate and PEIE were purchased from Sigama Aldrich, and PEDOT:F was purchased from Tenuc. The acceptor, L8-BO, was purchased from Solarmer. P(Qx8O-T) was synthesized following a previously reported procedure [49]. Unless otherwise specified, all chemicals were used without any further purification.

4.2 | Instrumental and Measurement Details

4.2.1 | Contact Angle

The contact angles of the active layer surfaces were measured with an Ossila Contact Angle Goniometer. The surface energy (γ) of the films and its dispersive (γ^d) and polar (γ^p) components were calculated using the Owens–Wendt model based on the contact angles of water and ethylene glycol. At least three different positions on each film were measured to ensure the accuracy of the data.

4.2.2 | In situ Photoluminescence (PL) and Absorption

In situ PL setup is similar to our previous work [18, 52]. In short, the polymer inks were coated on a precleaned glass substrate using a blade coater (Erichsen 510) with a moving blade (ZFR 2040). A 532 nm continuous wave laser diode was used to excite the wet polymer films, and an optical fiber was mounted on top of the resulting films to continuously collect emission signals to the spectrometer (QE-Pro, Ocean Optics). The integration time for every PL spectrum was set to be 100 ms. For the in situ absorption setup, a home-built stage was used to lift the glass substrate and the blade on top of the blade coater surface. An optical fiber was connected to a tungsten lamp (DH-2000, Ocean Optics) and mounted above the substrate to shine white light onto the polymer films. The transmitted signals from the polymer films were guided by another optical fiber, which was mounted below the substrate,

2367198x, 2026, 20, Downloaded from https://onlinelibrary.wiley.com/doi/10.1002/solr.70526 by Chalmers Research - Chalmers University Of Technology , Wiley Online Library on [29/10/2026]. See the Terms and Conditions (https://onlinelibrary.wiley.com/terms-and-conditions) on Wiley Online Library for rules of use; OA articles are governed by the applicable Creative Commons License

to the spectrometer. The integration time for every absorption spectrum was set to be 100 ms.

4.2.3 | ToF-SIMS

Measurements were performed with a ToF-SIMS (V system, ION-TOF). The primary beam was 25 keV $Bi3^+$ with a total current of 0.41 pA and a raster size of $50 \times 50\,\mu m^2$. O_2^+ ions were used with 1000 eV ion energy and 20 nA pulse current with a $200 \times 200\,\mu m^2$ raster size to bombard and etch the film. The collected secondary ion spectra were normalized to the total counts.

4.2.4 | Atomic Force Microscopy

AFM measurements were conducted on a Dimension Icon XR (Bruker) system, performed in Tapping mode under ambient conditions. The scanning area was set to $2 \times 2\,\mu m^2$, and the data were analyzed using NanoScope Analysis software to determine the RMS roughness.

4.2.5 | GIWAXS

GIWAXS measurements were performed using a Xeuss 3.0 system. The X-ray source was a Cu Kα radiation source (E = 8.05 keV, $\lambda = 1.54189$ Å). The scattering patterns were recorded on a Dectris Eiger2 R 1M detector with a pixel size of 75μm. The samples were measured in a vacuum chamber (< 1 mbar) to minimize air scattering. The sample-to-detector distance was calibrated to be 80 mm, and the beam center was located at (248.1, 1066.2) in pixel coordinates. Samples were prepared on Si substrates under the same conditions as those used for device fabrication.

4.3 | Device Fabrication

Devices were fabricated with a structure of glass/indium tin oxide (ITO)/Zn-PEIE/active layer/PEDOT:F/Ag. The glass/ITO substrate was first sonicated in DI water with detergent for 30 min, followed by cleaning with acetone and isopropyl alcohol (IPA) in an ultrasonic bath. This was followed by UV-ozone plasma for 20 min. Zn-PEIE with a thickness of approximately 30 nm was deposited by spin-coating at 3500 rpm for 30 s. Later, it was annealed in air for 10 min at 140 °C. In PPHJ device, the first layer of acceptor was then spin-coated atop ITO/Zn-PEIE from a solution of L8-BO with 9.6 mg mL^{-1} in o-xylene at 3500 rpm for 30 s in ambient conditions. A second layer of donor from a solution of P(Qx8O-T) with a concentration of 8 mg mL^{-1} in water-ethanol (15:85, volume ratio) was deposited, with everything else alike. The samples were put in vacuum chamber for 1 h and then transferred into the glove box. They were annealed at 100 °C for 5 min. In BHJ device, P(Qx8O-T) donor was blended with L8-BO in chloroform with an optimized donor:acceptor ratio of 1:1.2 (w/w) with a total concentration of 15.8 mg mL^{-1} at 50 °C for more than 1 h. The detailed optimization processes of BHJ film are listed in Table S3. Then, the active layer solution was spin-coated on top of the Zn-PEIE layer at 3000 rpm for 30 s in glovebox. The film thickness of the resulting active layer was determined to be 85–95 nm, and detailed data are listed in Table S4. Later, deposition of PEDOT:F (1 mg mL^{-1} in ethanol) was completed at 4000 rpm for 30 s atop the active layer. Finally, the top Ag electrode of 100 nm thickness was thermally evaporated through a mask with background pressure of 2×10^{-7} mbar. The devices were encapsulated using glass and epoxy adhesive before measurements.

4.4 | Characterization

4.4.1 | Current Density–Voltage (J–V) Curve

The *J–V* characteristics of the solar cells were measured using a Keithley 2400 source meter unit under AM1.5G (100 mW cm^{-2}) irradiation from a solar simulator (Newport MiniSol model LSH-7320). The *J–V* curves were measured from −2 to 2 V. The scan speed and dwell times were fixed at 0.05 V per step and 2 ms, respectively. The EQE spectra were measured using a QE-R solar cell spectral response measurement system (Enli Technology Co., Ltd., Taiwan).

4.4.2 | SCLC Measurement

The electron and hole mobilities of the acceptor/donor films were measured by using the SCLC method. The electron-only device with an architecture of ITO/Zn-PEIE/L8-BO/P(Qx8O-T)/PDINN/Ag and the hole-only device with an architecture of ITO/PEDOT:PSS/L8-BO/P(Qx8O-T)/PEDOT:F/Ag were fabricated. Mobility was determined by fitting the dark current to the model of a single-carrier SCLC, described by the equation

$$J = \frac{9\varepsilon_0\varepsilon_r\mu V^2}{8L^3}$$

where J is the current density, ε_0 is the vacuum permittivity, ε_r is the relative dielectric constant of the transport medium, μ is the charge carrier mobility, and L is the thickness of the active layer. The effective voltage is given by $V = V_{app} - V_{bi}$, where V_{app} is the applied voltage and V_{bi} is the built-in voltage. The mobility μ can be extracted from the slope of the $J^{0.5}$–V characteristics.

Acknowledgments

This work was supported by the Wallenberg Initiative Materials Science for Sustainability (WISE). J.X., M.F. and F.Z. acknowledge funding from Swedish Government Research Area in Materials Science on Functional Materials at Linkoping University Faculty Grant SFO-Mat-LiU No. 200900971. J.A. acknowledges funding from the European Union's Horizon Europe research and innovation program under grant agreement No 101147653. Y.L. thanks the supports from the Zhejiang Provincial Natural Science Foundation of China under Grant No. LQN26F040015 and the Non-profit Project of Science and Technology Department of Jiaxing (2024AY10036).

Funding

This work was supported by the Wallenberg Initiative Materials Science for Sustainability (WISE).

Data Availability Statement

The data that support the findings of this study are available from the corresponding author upon reasonable request.

2367198x, 2026, 20, Downloaded from https://onlinelibrary.wiley.com/doi/10.1002/solr.70526 by Chalmers Research - Chalmers University Of Technology , Wiley Online Library on [29/10/2026]. See the Terms and Conditions (https://onlinelibrary.wiley.com/terms-and-conditions) on Wiley Online Library for rules of use; OA articles are governed by the applicable Creative Commons License

References

1. G. Li, M. Al-Hashimi, A. Facchetti, and T. J. Marks, "Decoding the Halogenation Cost-Performance Paradox in Organic Solar Cells," *Nature Reviews Materials* 10 (2025): 617–631, https://doi.org/10.1038/s41578-025-00804-3.

2. J. Zhu, J. Xia, Y. Li, and Y. Li, "Perspective on Flexible Organic Solar Cells for Self-Powered Wearable Applications," *ACS Applied Materials & Interfaces* 17 (2025): 5595–5608, https://doi.org/10.1021/acsami.4c12238.

3. S. Li, Y. Wang, C. Sun, et al., "A General Elastomeric Agent to Addressing Embrittlement in High-Efficiency Organic Solar Cells," *Advanced Materials* 38 (2026): e16229, https://doi.org/10.1002/adma.202516229.

4. T. Wang, J. Fang, H. Zhang, et al., "Scalable Semitransparent Organic Solar Cells With Robust Film Thickness Tolerance for Building-Integrated Photovoltaics," *Nature Communications* 17 (2026): 2916, https://doi.org/10.1038/s41467-026-69537-3.

5. J.-Y. Fan, Z.-X. Liu, H. Chen, and C.-Z. Li, "Colorful and Semitransparent Organic Solar Modules via Air-Blade Assisted Coating of Active Layers," *Advanced Materials* 37 (2025): 2419525, https://doi.org/10.1002/adma.202419525.

6. C. Li, Y. Cai, P. Hu, et al., "Organic Solar Cells With 21% Efficiency Enabled by a Hybrid Interfacial Layer With Dual-Component Synergy," *Nature Materials* 24 (2025): 1626–1634, https://doi.org/10.1038/s41563-025-02305-8.

7. H. Chen, Y. Huang, R. Zhang, et al., "Organic Solar Cells With 20.82% Efficiency and High Tolerance of Active Layer Thickness Through Crystallization Sequence Manipulation," *Nature Materials* 24 (2025): 444–453, https://doi.org/10.1038/s41563-024-02062-0.

8. L. Wang, C. Chen, Z. Gan, et al., "Diluted Ternary Heterojunctions to Suppress Charge Recombination for Organic Solar Cells With 21% Efficiency," *Advanced Materials* 37 (2025): 2419923, https://doi.org/10.1002/adma.202419923.

9. J. Fu, H. Li, H. Liu, et al., "Two-Step Crystallization Modulated Through Acenaphthene Enabling 21% Binary Organic Solar Cells and 83.2% Fill Factor," *Nature Energy* 10 (2025): 1251–1261, https://doi.org/10.1038/s41560-025-01862-1.

10. Y. Xie, J. Tian, X. Yang, et al., "Thiophene Expanded Self-Assembled Monolayer as Hole Transport Layer for Organic Solar Cells With Efficiency of 20.78%," *Advanced Materials* 37 (2025): e02485, https://doi.org/10.1002/adma.202502485.

11. Y. Jiang, K. Liu, F. Liu, et al., "20.6% Efficiency Organic Solar Cells Enabled by Incorporating a Lower Bandgap Guest Nonfullerene Acceptor Without Open-Circuit Voltage Loss," *Advanced Materials* 37 (2025): 2500282, https://doi.org/10.1002/adma.202500282.

12. J. Xiang, Z.-X. Liu, H. Chen, and C.-Z. Li, " Robust and Sustainable Indium Anode Leading to Efficient and Stable Organic Solar Cells," *Advanced Materials* 35 (2023): 2303729, https://doi.org/10.1002/adma.202303729.

13. P. W. M. Blom, V. D. Mihailetchi, L. J. A. Koster, and D. E. Markov, "Device Physics of Polymer: Fullerene Bulk Heterojunction Solar Cells," *Advanced Materials* 19 (2007): 1551–1566, https://doi.org/10.1002/adma.200601093.

14. A. J. Heeger, "25th Anniversary Article: Bulk Heterojunction Solar Cells: Understanding the Mechanism of Operation," *Advanced Materials* 26 (2014): 10–28, https://doi.org/10.1002/adma.201304373.

15. S. Chandrabose, K. Chen, A. J. Barker, et al., "High Exciton Diffusion Coefficients in Fused Ring Electron Acceptor Films," *Journal of the American Chemical Society* 141 (2019): 6922–6929, https://doi.org/10.1021/jacs.8b12982.

16. D. Li, A. M. Kay, D. B. Riley, O. J. Sandberg, A. Armin, and P. Meredith, "Layer-by-Layer Processed Pseudo-Bilayer Heterojunctions Advance the Performance of Organic Solar Cells," *Advanced Energy Materials* 15 (2025): 2500816, https://doi.org/10.1002/aenm.202500816.

17. J. Cheng, C. Guo, L. Wang, et al., "Device Engineering of Non-Fullerene Organic Photovoltaics With Extrapolated Operational T80 Lifetime Over 45,000 h in Air," *Joule* 8 (2024): 2250–2264, https://doi.org/10.1016/j.joule.2024.05.014.

18. J. Xiang, S. Englund, Z. Genene, et al., "Situ Monitoring Drying Process to Disclose the Correlation Between the Molecular Weights of a Polymer Acceptor With a Flexible Spacer and the Performance of All-Polymer Solar Cells," *Journal of Materials Chemistry C* 12 (2024): 13029–13039, https://doi.org/10.1039/D4TC02217C.

19. J. Yuan, Y. Zhang, L. Zhou, et al., "Single-Junction Organic Solar Cell With Over 15% Efficiency Using Fused-Ring Acceptor With Electron-Deficient Core," *Joule* 3 (2019): 1140–1151, https://doi.org/10.1016/j.joule.2019.01.004.

20. L. Zhu, M. Zhang, J. Xu, et al., "Single-Junction Organic Solar Cells With Over 19% Efficiency Enabled by a Refined Double-Fibril Network Morphology," *Nature Materials* 21 (2022): 656–663, https://doi.org/10.1038/s41563-022-01244-y.

21. Z. Wen, R. Zhou, Z. Zheng, and Y. Zhao, "PM6/L8-BO Thin Films Through Layer-by-Layer Engineering: Formation Mechanism, Energetic Disorder, and Carrier Mobility," *Aggregate* 6 (2025): e729, https://doi.org/10.1002/agt2.729.

22. L. Wen, H. Mao, L. Zhang, et al., "Achieving Desired Pseudo-Planar Heterojunction Organic Solar Cells via Binary-Dilution Strategy," *Advanced Materials* 36 (2024): 2308159, https://doi.org/10.1002/adma.202308159.

23. D. He, J. Zhou, Y. Zhu, et al., "Manipulating Vertical Phase Separation Enables Pseudoplanar Heterojunction Organic Solar Cells Over 19% Efficiency via Ternary Polymerization," *Advanced Materials* 36 (2024): 2308909, https://doi.org/10.1002/adma.202308909.

24. J. Han, H. Xu, S. H. K. Paleti, et al., "Vertical Stratification Engineering of Insulating Poly(Aryl Ether)s Enables 18.6% Organic Solar Cells With Improved Stability," *ACS Energy Letters* 7 (2022): 2927–2936, https://doi.org/10.1021/acsenergylett.2c01586.

25. Q. Li, L.-M. Wang, S. Liu, et al., "Vertical Composition Distribution and Crystallinity Regulations Enable High-Performance Polymer Solar Cells With >17% Efficiency," *ACS Energy Letters* 5 (2020): 3637–3646, https://doi.org/10.1021/acsenergylett.0c01927.

26. Y. Wu, X. Dai, C. Liao, X. Xu, and Q. Peng, "Achieving Finely Optimized Morphology and Highly Efficient Layer-by-Layer Organic Solar Cells via Fluorinated Quinoxaline-Based Polymer Additives," *ACS Applied Materials & Interfaces* 17 (2025): 22760–22769, https://doi.org/10.1021/acsami.5c01556.

27. H. Chen, M. Deng, C. Li, et al., "Balanced Distribution of Donors and Acceptors Enabled by Volatile Isomerization Additives for 20.81% Efficiency Layer-by-Layer Polymer Solar Cells," *Energy & Environmental Science* 18 (2025): 8327–8338, https://doi.org/1039/D5EE02957K.

28. J. Wang, M. Deng, H. Chen, et al., "Minimizing Energy Loss by Designing Multifunctional Solid Additives to Independent Regulation of Donor and Acceptor Layers for Efficient LBL Polymer Solar Cells," *Advanced Science* 12 (2025): e2414712, https://doi.org/10.1002/advs.202414712.

29. J. Zhang, X. Dai, C. Liao, et al., "20.31% Efficiency Layer-by-Layer Organic Solar Cells Enabled by 3D Side-Chain Topology-Driven Dual-Fiber Interpenetrating Networks," *Advanced Materials* 38, 35, 2026), e73422 https://doi.org/10.1002/adma.73422.

30. Z. Yin, B. Wang, T. Huang, et al., "Breaking the Efficiency Bottleneck of Inverted Organic Solar Cells by Reversed Sequential Deposition," *Energy & Environmental Science*. (19, no. 8, 2026), 2597–2605 https://doi.org/10.1039/D5EE07561K.

31. B. Ma, Y. Yan, M. Wu, et al., "Sustainable Solution Processing Toward High-Efficiency Organic Solar Cells: A Comprehensive Review of Materials, Strategies, and Applications," *Advanced Functional Materials* 35 (2025): 2413814, https://doi.org/10.1002/adfm.202413814.

32. B. Guo, J. Li, K. Xiang, et al., "Isopropanol: A Green Solvent Additive for 20% Efficiency Organic Solar Cells With Excellent Generality and

2367198x, 2026, 20, Downloaded from https://onlinelibrary.wiley.com/doi/10.1002/solr.70526 by Chalmers Research - Chalmers University Of Technology , Wiley Online Library on [29/10/2026]. See the Terms and Conditions (https://onlinelibrary.wiley.com/terms-and-conditions) on Wiley Online Library for rules of use; OA articles are governed by the applicable Creative Commons License

Improved Eco-Compatibility," *Advanced Functional Materials* 36 (2026): e18732, https://doi.org/10.1002/adfm.202518732.

33. H. Chen, R. Zhang, X. Chen, et al., "A Guest-Assisted Molecular-Organization Approach for >17% Efficiency Organic Solar Cells Using Environmentally Friendly Solvents," *Nature Energy* 6 (2021): 1045–1053, https://doi.org/10.1038/s41560-021-00923-5.

34. J. Wan, L. Zeng, X. Liao, et al., "All-Green Solvent-Processed Planar Heterojunction Organic Solar Cells With Outstanding Power Conversion Efficiency of 16%," *Advanced Functional Materials* 32 (2022): 2107567, https://doi.org/10.1002/adfm.202107567.

35. X. Duan, J. Zhang, J. Kong, et al., "Over 20.5% Efficiency of Halogen-Free Solvent-Processed Organic Solar Cells Achieved by Anti-Solvent Strategy," *Advanced Materials* 38 (2026): e14076, https://doi.org/10.1002/adma.202514076.

36. R. Zeng, F. Han, W. Zhong, et al., "Lowering Toxicity of Solvent in Organic Solar Cells Manufacturing for 20% Efficiency," *Advanced Materials* 37 (2025): 2501812, https://doi.org/10.1002/adma.202501812.

37. X. Duan, J. Song, J. Zhang, et al., "Green Solvent-Processed Organic Solar Cells Approaching 20.4% Efficiency via Active Layer Pre-Solidification," *Advanced Materials* 37 (2025): 2503510, https://doi.org/10.1002/adma.202503510.

38. T. A. Dela Peña, R. Ma, W. Gao, et al., "Advancing Organic Photovoltaics Processed From Green-Solvents: From Characterization Methods to Optimization Strategies," *EnergyChem* 7 (2025): 100162, https://doi.org/10.1016/j.enchem.2025.100162.

39. H. He, X. Li, J. Zhang, et al., "Dynamic Hydrogen-Bonding Enables High-Performance and Mechanically Robust Organic Solar Cells Processed With Non-Halogenated Solvent," *Nature Communications* 16 (2025): 787, https://doi.org/10.1038/s41467-024-55375-8.

40. R. Zhang, H. Chen, T. Wang, et al., "Equally High Efficiencies of Organic Solar Cells Processed From Different Solvents Reveal Key Factors for Morphology Control," *Nature Energy* 10 (2025): 124–134, https://doi.org/10.1038/s41560-024-01678-5.

41. J. Wu, F. Sun, F. Hua, et al., "Balance Processing and Molecular Packing via Structural Disordering in a Random Terpolymer for Over 19% Efficiency Non-Halogenated Solvent Organic Solar Cells," *Advanced Energy Materials* 15 (2025): 2500024, https://doi.org/10.1002/aenm.202500024.

42. J. Wu, F. Sun, X. Xia, et al., "Over 18% Efficiency From Halogen-Free Solvent-Processed Polymer Solar Cells Enabled by Asymmetric Small Molecule Acceptors With Fluoro-Thienyl Extended Terminal," *Advanced Functional Materials* 35 (2025): 2423137, https://doi.org/10.1002/adfm.202423137.

43. L.-W. Feng, G. Li, S. Mukherjee, et al., "Green Solvent-Processable Trifluoromethylated π-Extended Non-Fullerene Acceptors for High-Efficiency Organic Solar Cells," *Energy & Fuels* 39 (2025): 7012–7020, https://doi.org/10.1021/acs.energyfuels.4c05715.

44. X. Chen, Y. Tian, A. Wupur, et al., "Donor–Acceptor Interaction Optimized Film-Forming Processes Lead to Efficient Organic Solar Cells and Modules Fabricated With Non-Halogenated Solvents," *Angewandte Chemie* 137 (2025): e202515280, https://doi.org/10.1002/ange.202515280.

45. S. Lee, Y. Kim, Z. Wu, et al., "Aqueous-Soluble Naphthalene Diimide-Based Polymer Acceptors for Efficient and Air-Stable All-Polymer Solar Cells," *ACS Applied Materials & Interfaces* 11 (2019): 45038–45047, https://doi.org/10.1021/acsami.9b13812.

46. L. Shang, S. Qu, Y. Deng, et al., "Simple Furan-Based Polymers With the Self-Healing Function Enable Efficient Eco-Friendly Organic Solar Cells With High Stability," *Journal of Materials Chemistry C* 10 (2022): 506–516, https://doi.org/10.1039/D1TC05111C.

47. R. B. Ribeiro, L. R. Franco, A. Holmes, et al., "Assessing Structural and Optical Properties of PTQ10-Based Donor Polymers in Solution for Eco-Friendly Photovoltaics: A Multiscale Modeling Study," *The Journal of Physical Chemistry B* 129 (2025): 5887–5900, https://doi.org/10.1021/acs.jpcb.5c01972.

48. J. Neu, S. Samson, K. Ding, J. J. Rech, H. Ade, and W. You, "Oligo(Ethylene Glycol) Side Chain Architecture Enables Alcohol-Processable Conjugated Polymers for Organic Solar Cells," *Macromolecules* 56 (2023): 2092–2103, https://doi.org/10.1021/acs.macromol.2c02259.

49. T. T. Filate, S. Lee, L. R. Franco, et al., "Aqueous Processed All-Polymer Solar Cells With High Open-Circuit Voltage Based on Low-Cost Thiophene–Quinoxaline Polymers," *ACS Applied Materials & Interfaces* 16 (2024): 12886–12896, https://doi.org/10.1021/acsami.3c18994.

50. J. Chen, X. Zhou, X. Liu, Q. Luo, K. Feng, and Y. Zhou, "Adsorbate Engineering on ZnO for Ultraviolet Light Activation-Free Organic Photovoltaic Modules," *Solar RRL* 8 (2024): 2400164, https://doi.org/10.1002/solr.v8.11.

51. Y. Jiang, X. Dong, L. Sun, et al., "An Alcohol-Dispersed Conducting Polymer Complex for Fully Printable Organic Solar Cells With Improved Stability," *Nature Energy* 7 (2022): 352–359, https://doi.org/10.1038/s41560-022-00997-9.

52. Y. Liu, A. Yangui, R. Zhang, et al., "In Situ Optical Studies on Morphology Formation in Organic Photovoltaic Blends," *Small Methods* 5 (2021): 2100585, https://doi.org/10.1002/smtd.202100585.

Supporting Information

Additional supporting information can be found online in the Supporting Information section.

2367198x, 2026, 20, Downloaded from https://onlinelibrary.wiley.com/doi/10.1002/solr.70526 by Chalmers Research - Chalmers University Of Technology , Wiley Online Library on [29/10/2026]. See the Terms and Conditions (https://onlinelibrary.wiley.com/terms-and-conditions) on Wiley Online Library for rules of use; OA articles are governed by the applicable Creative Commons License